



Cite this: *Dalton Trans.*, 2014, **43**, 14787

Role of morphology in the performance of $\text{LiFe}_{0.5}\text{Mn}_{1.5}\text{O}_4$ spinel cathodes for lithium-ion batteries†

M. P. Pico,* I. Álvarez-Serrano, M. L. López and M. L. Veiga

Spinel oxides with composition $\text{LiMn}_{2-x}\text{M}_x\text{O}_4$ (M, a transition metal) are intensively studied due to their remarkable electrochemical properties. This study deals with cathode materials based on the lithium iron manganese oxide $\text{LiFe}_{0.5}\text{Mn}_{1.5}\text{O}_4$ synthesized by different methods (sol-gel, in solution and hydrothermal) in order to obtain samples with various morphologies. SEM results show microspheres, composed of nanosized/submicrometer-sized subunits, microrods with a less porous surface, and finally nanoparticles that form micro-sized aggregates. The samples obtained by both solution and hydrothermal methods provided the best electrochemical behavior. In all cases, the coulombic efficiency is around 90%, and it remains constant during the tested cycles. Specific capacities remain stable between 95% and 98% of capacity retention after series of cycles in samples formed by microspheres or micro-size aggregates. These values are notably higher than those obtained for the samples with particles of heterogeneous size (49%). A $\text{LiMn}_{1.5}\text{Fe}_{0.5}\text{O}_4/\text{Li}_2\text{MnO}_3$ composite has been prepared by the solvothermal technique in order to increase its capacity and energy density. These cells show a good cyclability at different current densities. All cells based on these $\text{LiFe}_{0.5}\text{Mn}_{1.5}\text{O}_4$ cathodes recover their discharge capacity when the current density returns to C/10.

Received 17th June 2014,
Accepted 5th August 2014

DOI: 10.1039/c4dt01809e

www.rsc.org/dalton

1. Introduction

Nowadays, energy and environment are the two most challenging issues faced by our society. Batteries are particularly interesting portable power sources, commonly used in household and industrial applications such as energy storage and management.^{1,2} Among various existing batteries, rechargeable lithium batteries have considerable advantages for the development of energy devices because of their high energy density, long life cycle, and cost effectiveness, as well as they are long lasting and environmentally friendly.^{3,4} Thus, lithium-ion batteries can be considered to be the most impressive success story of modern electrochemistry in the last two decades.⁵

The material for a cathode of a rechargeable battery should be capable of reversibly insert/deinsert Li ions at a large capacity and high potential, and should undergo minimal structural changes during this process for an acceptable cycle performance. Among the most promising Li-insertion compounds, the manganese-spinel $\text{Li}_{1-x}\text{Mn}_2\text{O}_4$ is now used as 4.0 V positive-electrode material in rechargeable lithium batteries because of its abundance, low cost and environment friendliness, although several drawbacks have impeded its general use. The major drawback of LiMn_2O_4 phase is related to its high content of Jahn-Teller Mn^{3+} ions, which dismute into Mn^{4+} and the highly soluble Mn^{2+} . As a consequence of this effect, there is a 16% elongation of the *c*-axis upon phase conversion, which causes fracturing and disconnection of particles, which results in a rapid capacity fading upon cycling at room temperature. Removal of Li from the tetrahedral sites to form the delithiated phase, MnO_2 , is much more reversible and occurs above 4 V vs. Li/Li^+ as cycling is restricted to the 4 V region.^{6,7} However, this problem can be partially solved through cationic substitution with different metal cations (*e.g.*, Al, Ti, Cr, Fe, Co, Ni, Cu), giving better performance characteristics than LiMn_2O_4 .⁸⁻¹⁰ In particular, intensive efforts have been focused on the very promising development of the spinel $\text{LiNi}_{0.5}\text{Mn}_{1.5}\text{O}_4$ and its variants as cathode materials for high-energy lithium-ion batteries.¹¹ In comparison with LiMn_2O_4 ,

Dpto. Química Inorgánica I, Facultad de Ciencias Químicas, Universidad Complutense de Madrid, 28040 Madrid, Spain. E-mail: mppico@ucm.es

† Electronic supplementary information (ESI) available: S1–S5: X ray diffraction pattern and scanning microscopy image of MnCO_3 and MnO_2 . S6: X ray diffraction pattern of Mn-EG and Fe-EG. S7: (a) Thermogravimetric analysis of Mn-EG and Fe-EG. (b) X-ray diffraction pattern of residue. S8: Scanning microscopy image of $\text{Mn}_{2-x}\text{Fe}_x\text{O}_3$. S9: EELS spectra for the SG sample: (a) Mn L_{2,3} and (b) Fe L_{2,3} edges. S10: Charge/discharge curves at rate of C/5 between 3–5 V for $\text{LiMn}_{1.5}\text{Fe}_{0.5}\text{O}_4$ prepared by different method. S11: Charge/discharge curves at a rate C/5 for $\text{LiMn}_{1.5}\text{Fe}_{0.5}\text{O}_4/\text{Li}_2\text{MnO}_3$ composite cathodes. See DOI: 10.1039/c4dt01809e

manganese remains essentially as Mn^{4+} in octahedral sites under normal cycling conditions, thus avoiding the Jahn–Teller distortion of Mn^{3+} ions. Different methods of synthesis^{12,13} show that $\text{LiNi}_{0.5}\text{Mn}_{1.5}\text{O}_4$ is formed together with impurities of $\text{Li}_{1-x}\text{Ni}_x\text{O}$ rocksalt-type, although its electrochemical characteristics, such as high discharge potential, excellent rate capability and good cyclability, seem to be of great interest. Nevertheless, the high operating potential may require the use of specially designed electrolytic solutions and coatings on particle surfaces to reduce coulombic inefficiencies and to extend life cycle. As it occurs with the LiMn_2O_4 variants, dissolution of Mn is a potential problem for life cycle.

On the other hand, in order to avoid the problem of nickel toxicity, the $\text{LiFe}_{0.5}\text{Mn}_{1.5}\text{O}_4$ spinel is an excellent candidate due to its lower cost and lesser toxicity in comparison with similar transition metal materials. Moreover, preliminary electrochemical studies show that the $\text{LiFe}_{0.5}\text{Mn}_{1.5}\text{O}_4$ spinel presents excellent electrochemical properties of as a 5 V cathode material.^{14,15} In this study, the preparation of $\text{LiFe}_{0.5}\text{Mn}_{1.5}\text{O}_4$ spinel by different methods to use them as cathode materials for Li-ion batteries is reported. Furthermore, we have characterized these materials from a structural and electrochemical point of view, and show how the results are related to the morphology of the samples. To the best of our knowledge, such a detailed study of this material has not been reported before.

2. Experimental

2.1. Synthesis

The $\text{LiFe}_{0.5}\text{Mn}_{1.5}\text{O}_4$ spinel was synthesized by different methods in order to modulate the morphology of the samples obtained.

(a) Synthesis by “liquid mix” method. Polycrystalline powders of $\text{LiFe}_{0.5}\text{Mn}_{1.5}\text{O}_4$ were synthesized by a sol–gel method (SG hereafter), starting from the required amounts of LiNO_3 (Merck), $\text{Mn}(\text{NO}_3)_2 \cdot 4\text{H}_2\text{O}$ (Merck) and $\text{Fe}(\text{NO}_3)_3 \cdot 9\text{H}_2\text{O}$ (Panreac) dissolved in deionized water. After that, nitric acid, citric acid monohydrate and ethylene glycol were added and the solution was heated and stirred. Dark brown solids were obtained after this process. A further thermal treatment at 400 °C for a week was applied to obtain pure phases, and then, the sample was heated for a week at 600 °C.¹⁶

The following methods were used to obtain the precursor materials that will be used as a template.

(b) Synthesis by solution method (known in the literature as impregnation method.¹⁷) Modified versions of this impregnation method were used to prepare two different samples of shape-controlled MnCO_3 precursor, which were then calcined to yield the textured MnO_2 powders. These powders were further treated with the lithium and iron nitrates to obtain two different spinel samples. On the one hand, the precursor MnCO_3 was obtained by a previously reported precipitation method, in which minor modifications have been introduced.¹⁸ In brief, $\text{MnSO}_4 \cdot \text{H}_2\text{O}$ and NH_4HCO_3 were separately dissolved in distilled water. Then, ethanol and the NH_4HCO_3

solution were added to the $\text{MnSO}_4 \cdot \text{H}_2\text{O}$ solution in sequence under stirring. The mixture was stirred for 1 h at room temperature and then centrifuged, washed with water and ethanol three times. Note that the product obtained was dried at 80 °C. X-ray diffraction (XRD) pattern shown in Fig. S1† confirms that the product is MnCO_3 . These particles have a spherical shape, as shown by scanning electron microscopy (Fig. S2a†).

On the other hand, some amount of $(\text{NH}_4)_2\text{SO}_4$ was also added to the initial $\text{MnSO}_4 \cdot \text{H}_2\text{O}$ solution and the precipitation was performed by maintaining the mixture at 50 °C for 9 h; in these conditions, the MnCO_3 microspheres obtained were greater in size (Fig. S2b†).

Highly porous MnO_2 microspheres were synthesized by thermal decomposition of the above described MnCO_3 microspheres at 400 °C for 12 h (Fig. S3 and S4†). These MnO_2 samples were mixed with LiNO_3 and $\text{Fe}(\text{NO}_3)_3 \cdot 9\text{H}_2\text{O}$ and heated at 700 °C for one week, yielding the spinel-type samples labelled as Imp_1 and Imp_2 hereafter. In this step, LiNO_3 and $\text{Fe}(\text{NO}_3)_3 \cdot 9\text{H}_2\text{O}$ are introduced into mesopores of the MnO_2 microspheres by a simple impregnation method. The reactions that take place in this process have been already described by Goodenough *et al.*²⁷

(c) Template method (TM). The aim of this method is to obtain MnO_2 rods by hydrothermal reactions to be used as a precursor. MnO_2 rods were synthesized by a previously reported procedure.¹⁹ Analytical grade $\text{Mn}(\text{CH}_3\text{COO})_2 \cdot 4\text{H}_2\text{O}$ (99.99% Aldrich), $\text{Na}_2\text{S}_2\text{O}_8$ ($\geq 98\%$ reagent grade, Sigma-Aldrich) and deionized water were used without further purification. In a typical synthesis, $\text{Mn}(\text{CH}_3\text{COO})_2 \cdot 4\text{H}_2\text{O}$ and $\text{Na}_2\text{S}_2\text{O}_8$ were dissolved at room temperature with a molar ratio of 1 : 1 in 80 mL of distilled water by magnetic stirring to form a homogeneous clear solution. This solution was transferred to a 50 mL Teflon-lined stainless steel autoclave and heated at 120 °C for 12 h in an electric oven for the hydrothermal reaction. After the reaction, the final precipitated products were washed sequentially with deionized water and ethanol to remove the sulfate ions and other remnants by filtration. The powder obtained was subsequently dried at 100 °C for 12 h in air. The corresponding XRD pattern is shown in Fig. S5,† and it is the main characteristic of MnO_2 rutile. These MnO_2 rods were then used as a template. Thus, stoichiometric amounts of MnO_2 rods, LiNO_3 and $\text{Fe}(\text{NO}_3)_3 \cdot 9\text{H}_2\text{O}$ were mixed and heated at 700 °C for 24 h in alumina crucibles.

(d) Solvothermal synthesis (SS). The synthesis procedure is based on the method used by Hu *et al.*²⁰ These authors described the preparation of CoMn_2O_4 hierarchical microspheres assembled with porous nanosheets by a solvothermal synthesis, followed by a thermal decomposition. In our case, the first step, consists in precipitating Mn and Fe alkoxide powders from ethanediol solutions of the respective salts. Later, the powder obtained is mixed with a stoichiometric amount of LiNO_3 , and the following thermal decomposition leads to a crystalline spinel.

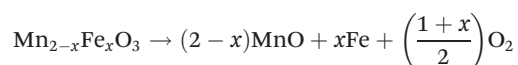
In a typical synthesis, $\text{Mn}(\text{CH}_3\text{COO})_2 \cdot 4\text{H}_2\text{O}$ (99.99% Aldrich) and $\text{Fe}(\text{CH}_3\text{COO})_2$ (95% Aldrich) in stoichiometric ratio were dissolved at room temperature in ethylene glycol

(99% Panreac), as well as polyethylene glycol 1000 (99% Panreac). Magnetic stirring was applied to form a homogeneous clear solution. Ethylene glycol (EG) is an optimal solvent that presents good coordination ability, and serves as a ligand to form coordination complexes with several metallic cations upon heating.²⁰ The mixed solution was transferred into a 50 mL Teflon-lined stainless steel autoclave and heated up to 200 °C for 12 h in an electric oven for the hydrothermal reaction. After the reaction, the final precipitated products were washed sequentially with deionized water and ethanol and the powder obtained was subsequently dried at 100 °C for 12 h in air. Immediately after this, LiNO₃ (98% Merck) was added in a stoichiometric proportion. The mixture was heated in a furnace at 700 °C during 33 h.

The precursor phase formed in the solvothermal reaction was characterized by XRD. Fig. S6† shows the crystallinity of the precursor, which is similar to that shown by Mn-EG²¹ and Fe-EG.²² The strong peak around $2\theta = 10^\circ$ is characteristic of products formed during polyol-mediated processes.²⁰ In this case, it could correspond to the formation of metal glycolates or alkoxide derivatives by alcoholysis and coordination of ethylene glycol with the metal ions as (CH₂)₂(O)₂Mn and (CH₂)₂(O)₂Fe.

Furthermore, the precursor was characterized by thermogravimetric analysis (TG), as shown in Fig. S7a,† in which a weight loss around 31(1)% is achieved at 600 °C under an oxygen atmosphere, which is typical of this kind of products.²¹ The TG residue was characterized and the XRD pattern is shown in Fig. S7b.† All the diffraction peaks could be indexed on the basis of phase Mn_{2-x}Fe_xO₃ (JCPDS no. 24-507).

In order to obtain the Mn and Fe content in this phase, a TG analysis under 3He : 2H₂ atmosphere was carried out with a heating rate of 3 °C min⁻¹ up to 600 °C. The XRD pattern of the residue (not shown) allowed us to identify the final products of the reduction process and settle the reaction expressed below:



The experimental weight loss was around 17(1)% and the deduced composition of this phase was Mn_{1.3}Fe_{0.7}O₃. The corresponding Mn/Fe ratio is 1.9(4), which is lower than the theoretical value. Moreover, the Mn/Fe ratio determined by energy-dispersive X-ray spectroscopy (EDX) analysis is 1.9(5) instead of 3, which is in good agreement with the TG results carried out under hydrogen atmosphere.

Fig. S8† shows representative images obtained by scanning electron microscopy (SEM) of Mn_{2-x}Fe_xO₃ after heating the precursor at 600 °C. These images reveal that the product is mostly composed by spherical particles with diameters ranging from 50 to 150 nm (Fig. S8a†). These particles seem to be agglomerates that give rise to different morphologies (Fig. S8b†). Nanosheets with thickness of around 50 nm and width of around 2 μm (Fig. S8c and S8d†) are also observed. Moreover, the surfaces of these particles are highly porous,

similar to those obtained by means of the impregnation method described above.

Finally, LiFe_{0.5}Mn_{1.5}O₄ was obtained by mixing stoichiometric amounts of LiNO₃ and the metal-alkoxide precursor at 700 °C during 33 h. The samples prepared by this method will be labelled SS hereafter.

2.2. Characterization

All the samples obtained were identified by XRD at room temperature, and the data were refined using the Rietveld method and FULLPROF software.²³ The XRD patterns were recorded with a Philips X'Pert MPD diffractometer with a PW 3050/00 goniometer, using Ni filtered Cu Kα and 2 step size of 0.05° with a counting time of 12.5 s for each step. The goniometer was connected to a PC controlled by the commercial program PCAPD.

Electron energy loss spectroscopy (EELS) experiments were performed using a JEOL JEM 3000F microscope operating at 300 kV, with an ENFINA spectrometer with an energy resolution of 1.3 eV. EELS spectra were acquired for the L_{2,3} edge of the transition metals.

Thermogravimetric (TG) data under O₂ atmosphere were obtained by a Perkin Elmer Pyris thermogravimeter at 10 K min⁻¹ heating/cooling rate. TG analyses in reductive conditions were carried out under a H₂/He (300 mbar/200 mbar) atmosphere using a Cahn D-200 electrobalance. This device is equipped with a furnace and a two-channel register allowing the simultaneous recording of the weight loss and the temperatures.

Scanning electron microscopy (SEM) images were obtained with a JEOL JSM 6335F microscope. The porous structure of the samples was determined by N₂ adsorption-desorption at -196 °C, performed in a SA 3100 surface area analyzer (Beckman Coulter). Samples were previously outgassed for at least 4 hours at 100 °C, before and after adsorption. From the N₂ isotherm ($P/P_0 = 0.98$), the apparent surface area was determined by applying the BET equation. The pore volume (V_p) and mean pore diameter (d_p) were also obtained from the N₂ isotherm data.

Electrochemical charge/discharge curves were measured using Swagelok® cells. Cathodes were prepared by mixing 80 wt% synthesized samples, 15 wt% extra pure carbon and 5 wt% polyvinylidene fluoride (PVDF). The resulting electrodes had an active material loading of around 10–15 mg. The mixture was pressed to obtain a circular tablet. The electrolyte employed was ethylene carbonate (EC)–diethyl carbonate (DEC) (50/50) 1 M-LiPF₆ soaked up in a carbon microfiber disk. Lithium metal was the anode. Cells were packed under a purified Ar atmosphere.

3. Results and discussion

3.1. Structural and microstructural studies

The XRD patterns of LiFe_{0.5}Mn_{1.5}O₄ obtained with different synthesis methods are shown in Fig. 1. All these patterns

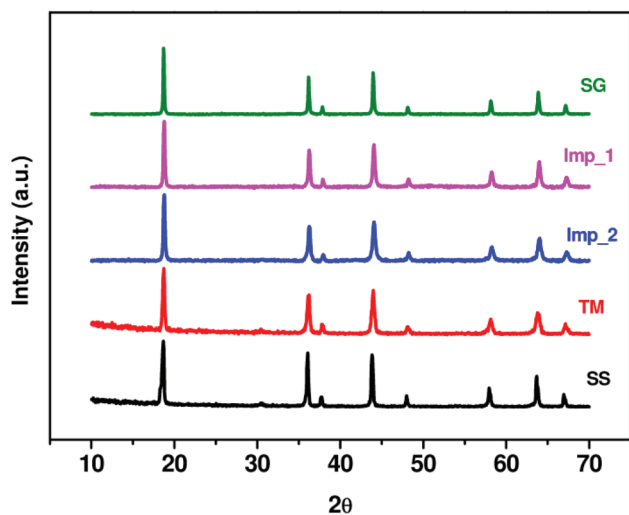


Fig. 1 XRD patterns of the $\text{LiFe}_{0.5}\text{Mn}_{1.5}\text{O}_4$ particles.

exhibit the characteristic diffraction lines of a single pure cubic spinel structure without any detectable impurity. In general, the samples are highly crystalline without any displacements in the respective 2θ values. On the other hand, the narrowest peaks correspond to particles obtained by the sol-gel synthesis.

The XRD data for all the phases were analyzed by the Rietveld method and refined in the $Fd\bar{3}m$ space group with Li cations located in the tetrahedral sites (8a) and the Fe/Mn cations randomly distributed in the octahedral sites (16d). Fig. 2a and 2b show the calculated and observed diffraction profiles of SG at 600 °C and Imp_1 at 700 °C, as well as the differences between them. Similar results have been obtained for the remaining samples. In all cases, the differences between the experimental and calculated profiles and the R factors obtained indicate the validity of the model proposed.

The cell parameters obtained in the refinement do not vary significantly with the synthesis method, ranging from 8.248(1) to 8.237(2) Å for the SG and Imp samples, respectively.

Table 1 Mn/Fe ratio obtained by EDX and textural characteristic for all samples

Sample	Mn/Fe ratio	S_{BET} ($\text{m}^2 \text{g}^{-1}$)	D_p (nm)	V_p (mL g^{-1})
SG	2.7	11	4.3	0.04
Imp_1	3.1	8	3.7	0.03
Imp_2	3.0	7	4.3	0.03
TM	2.9	7	4.3	0.06
SS	1.9	5	4.7	0.03

The Mn/Fe ratio determined by EDX analysis is around 3 in all cases (apart from SS sample), which perfectly agrees with the nominal composition of $\text{LiFe}_{0.5}\text{Mn}_{1.5}\text{O}_4$ within the experimental error, as shown in Table 1. However, the sample prepared by SS method shows a Mn/Fe of 1.9, which is lower than the nominal one. Similar values are obtained by EDX for the SS sample heated at 600 °C, and they are in agreement with those achieved by TG analysis under H_2 :He atmosphere, as has been mentioned before. Therefore, in the SS method, the sample composition can be considered as $\text{LiFe}_{0.7}\text{Mn}_{1.3}\text{O}_4$.

EELS experiments were carried out in order to obtain complementary information about the oxidation states of Mn and Fe. Fig. S9† shows, as a representative example, the EELS spectra in both the $L_{2,3}$ Mn and Fe edges (S9a and S9b, respectively) for the SG sample. It has previously been pointed out²⁴ that based on the ratio of the peaks intensities is an adequate technique to estimate the Mn oxidation state, but the chemical shift method is more accurate for analyzing the oxidation state of iron.

Taking into account that the typical values of the Fe $L_{2,3}$ edge signals have been reported to be *ca.* 708/722 eV for Fe^{2+} and 711/724 eV for Fe^{3+} (ref. 24 and 25) the trivalent oxidation state for Fe cations in the samples can be assumed. On the other hand, the $L_{2,3}$ ratios for the Mn window, roughly estimated from intensity increments, together with the observed shift, are consistent with a mixed valence $\text{Mn}^{4+}/\text{Mn}^{3+}$. Thus, EELS experiments allowed us both to ascribe a trivalent oxidation state for Fe cations and to confirm the expected mixed valence, between +3 and +4, for Mn cations.

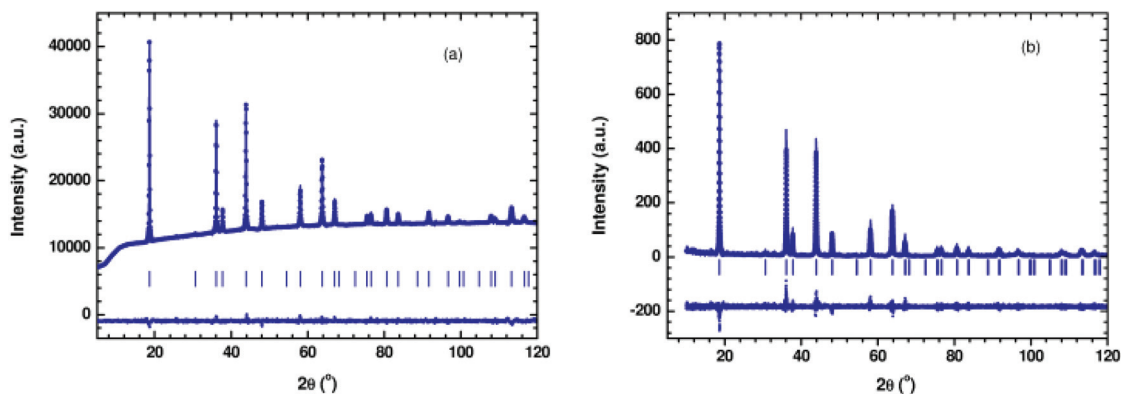


Fig. 2 Structural refinement for $\text{LiMn}_{1.5}\text{Fe}_{0.5}\text{O}_4$: (a) SG sample; (b) Imp sample. Observed patterns are denoted by solid lines, and the calculated and difference plots are shown by dots. Reflection positions for spinel phases are included (bars).

Recently, it has been pointed out that the specific surface area and the pore size of the samples are strongly related to the electrochemical behavior. This is due to this fact that porosity facilitates the transport of Li ions and it is critical to the rate capability.²⁶ In order to study the porosity of these samples, their textural properties have been obtained by nitrogen adsorption at 77 K (Fig. 3). BET surface area data have been calculated and are summarized in Table 1, together with the pore size distribution and pore volume of all the samples. As can be observed, S_{BET} varies between 5 and 11, D_p changes between 3.7 and 4.7, and V_p is around 0.03 in all samples. The SG sample exhibits the highest S_{BET} and pore volume, and the SS shows the highest pore diameter. Nevertheless, these variations in textural parameters are not significant.

Fig. 4 shows SEM images of $\text{LiFe}_{0.5}\text{Mn}_{1.5}\text{O}_4$ particles obtained under different conditions. The SEM results for the sample SG are shown in Fig. 4a and 4b, where highly agglomerated crystalline particles, together with grains with heterogeneous sizes can be appreciated. In contrast, a very different situation is found for samples obtained by impregnation methods. The lowest-magnification images (Fig. 4c and 4e) reveal that the product is composed of uniform microspheres with diameters of around 1 and 2 μm , depending on the impregnation method used, Imp_1 and Imp_2, respectively.

Fig. 4d and 4f show that the $\text{LiFe}_{0.5}\text{Mn}_{1.5}\text{O}_4$ microspheres have a rough surface, suggesting that the walls of these particles are highly porous and they are composed of nanosized/submicrometer-sized subunits. Moreover, from the broken part of a microsphere, the hollow nature of microspheres can be identified unambiguously (Fig. 4f). Interestingly, when the TM method is used, particles show rod-like morphology with uniform sizes between 2 and 2.5 μm in length and $\sim 0.4 \mu\text{m}$ in width. Another important difference with the previous samples is that these microrods show a smoother surface; therefore, the particles are less porous, as can be easily appreciated in Fig. 4h.

Finally, Fig. 4i–4k show the images of the samples prepared by the SS method at lower and higher magnification. Fig. 4i

shows that this sample consists of nanoparticles that are agglomerated and form micro-sized aggregates with different morphologies. The main feature is the formation of pseudo-spheres with a diameter near to 500 nm that results in closing circular sheets (see arrows in Fig. 4j). In the image of the highest magnification (Fig. 4k) the connection between nanoparticles can be observed.

Taking into account that the $\text{LiFe}_{0.5}\text{Mn}_{1.5}\text{O}_4$ samples prepared by different methods exhibit very similar textural properties, their electrochemical behaviour will presumably be related to the morphology found for these materials.

3.2. Electrochemical characterization

In order to evaluate their electrochemical properties, the samples with different morphologies were cycled at several charge/discharge rates over a potential window of 3–5 V.

Fig. 5 shows the first charge/discharge voltage profiles for all samples at $C/10$. These cycles exhibit two plateaus at 4 and 5 V, which can be related to $\text{Mn}^{4+}/\text{Mn}^{3+}$ (ref. 27) and $\text{Fe}^{4+}/\text{Fe}^{3+}$ couples,²⁸ respectively. The experimental capacities in the first cycle are shown in Table 2. None of the samples reaches the theoretical capacity value of the $\text{LiFe}_{0.5}\text{Mn}_{1.5}\text{O}_4$ electrode (148 mA h g^{-1}). In these samples only up to half of the de-inserted lithium can be attributed to the $\text{Mn}^{4+}/\text{Mn}^{3+}$ couple (only up to 0.5 Mn^{3+} per formula unit is present in the samples) and at least the other half is due to the $\text{Fe}^{4+}/\text{Fe}^{3+}$ couple. In Table 2, it can be observed that a capacity value close to 70 mA h g^{-1} is reached only in SG and TM samples at the 4 V plateau. A different situation is obtained in the 5 V plateau. In all cases, values close to 20 mA h g^{-1} have been achieved because a partial oxidation of Fe^{3+} has occurred. Actually, the process related to the $\text{Fe}^{4+}/\text{Fe}^{3+}$ redox couple takes place in a plateau centered at 5 V. Consequently, it is necessary to increase the voltage value at least up to 5.3 V in order to oxidize completely the Fe content. This voltage is too high; therefore, electrolyte oxidation processes in the surface electrode/electrolyte could take place.²⁹ For these reasons, the voltage window employed in this work was fixed in the 3–5 V range. Only in one case the voltage was increased with the aim

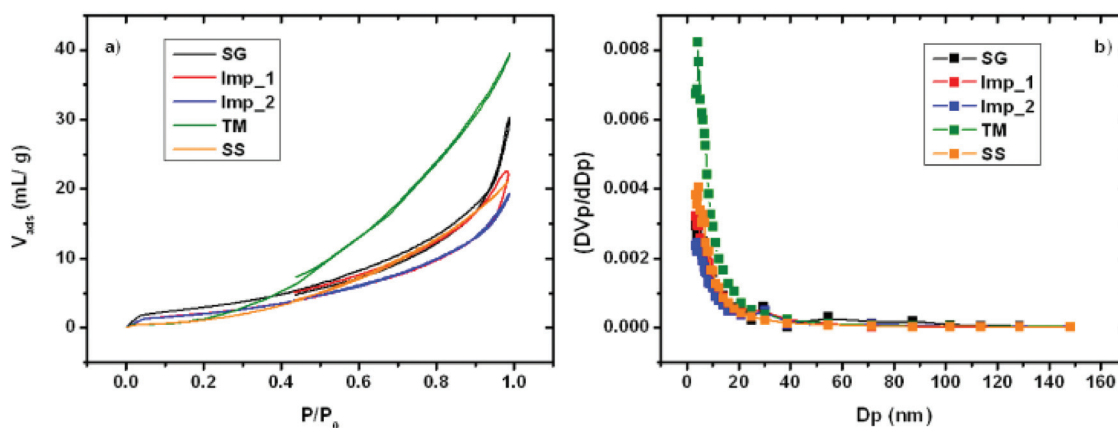


Fig. 3 Textural characterization: (a) nitrogen adsorption–desorption isotherms; (b) pore size distribution.

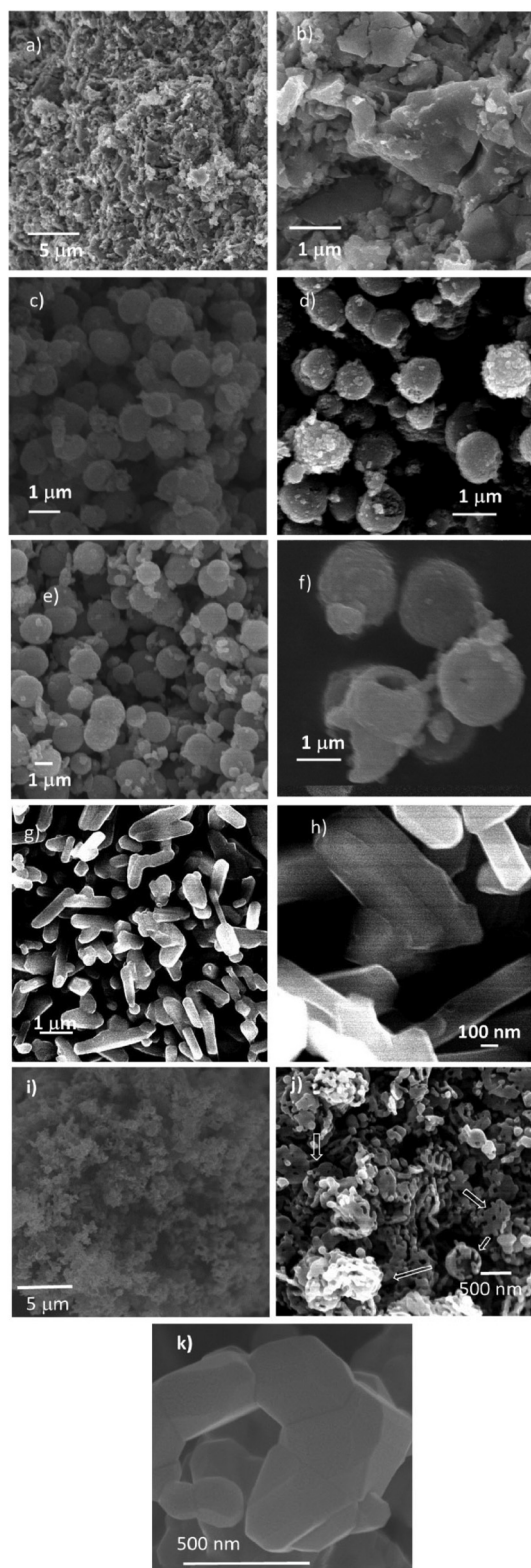


Fig. 4 SEM images of $\text{LiFe}_{0.5}\text{Mn}_{1.5}\text{O}_4$ samples at different magnifications: (a) and (b) SG; (c) and (d) Imp_1; (e) and (f) Imp_2; (g) and (h) TM; (i), (j) and (k) SS samples. SEM images of $\text{LiFe}_{0.5}\text{Mn}_{1.5}\text{O}_4$ samples at different magnifications: (a) and (b) SG; (c) and (d) Imp_1; (e) and (f) Imp_2; (g) and (h) TM; (i), (j) and (k) SS samples. Arrows in (j) indicate closed sheets (see text).

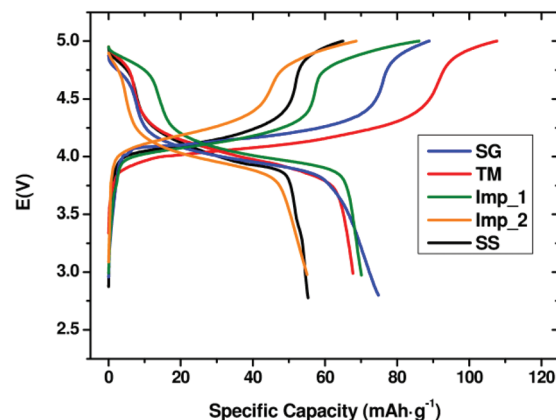


Fig. 5 The first discharge/charge cycles at C/10 for all samples.

of observing the role of Fe^{4+} over the electrolyte/electrode surface.

Fig. 5 and Table 2 show that the amount of inserted Li^+ (*i.e.* Q_i 4 V) is practically the same for all the samples except for the SS one (where the Mn/Fe ratio is the smallest), which gives the lowest values and shows a narrower plateau at 4 V. Table 2 also shows the coulombic efficiency for this first stage. The best results correspond to the Imp samples, where the amounts of Li deinserted in the 5 V process are the highest. These samples exhibit more homogenous sizes, and they are constituted by micrometric particles formed by nanometric units (see Fig. 4c–f).

In order to match the electrochemical behaviors with the respective morphologies, Fig. 6 gathers the results of the cycle tests at C/10 for all the samples, together with the discharge capacity *versus* cycle number at various current densities. In the SG sample, the discharge capacity decreases quickly and a 50% of capacity is loss in the 10th cycle. This capacity fade is clearly related to the plateau at 4 V; therefore, it can be attributed to the Mn dissolution in the electrolyte.³⁰ Moreover, the small plateau at 5 V quickly diminishes and in the second cycle this plateau practically disappears. The sample prepared by the SG method consists of heterogeneous particles without a defined morphology (Fig. 4a). A different situation can be observed with the remaining samples, for which the fading at 4 V operating is practically not observed, and the decrease in the capacity is related to the 5 V plateau, which is progressively smaller as the number of cycles increases. Eftekhari *et al.*^{14,15} conclude that a decrease at 5 V is due to the direct reaction of organic species present in the electrolyte with the high-valent Fe over the electrolyte/electrode interface. In particular, when the electrochemical cell composed with $\text{LiMn}_{1.5}\text{Fe}_{0.5}\text{O}_4$ -Imp as cathode was cycled at higher rate, *i.e.* C/5 (see Fig. S10, ESI†), the highest voltage plateau almost disappears and, as a consequence, the capacity losses are very low (2%, with sizes around 1 μm) or even negligible (with sizes around 2 μm) in these spherical morphologies. It is interesting to note that the discharge capacity is recovered when the rate is diminished again (Fig. 6c).

Table 2 Experimental specific capacities (deinsertion, Q_D , and insertion, Q_i) and coulombic efficiency ($100 \times Q_i/Q_D$) for $\text{LiFe}_{0.5}\text{Mn}_{1.5}\text{O}_4$

Sample	Q_D (mA h g^{-1})	Q_D 4 V (mA h g^{-1})	Q_D 5 V (mA h g^{-1})	Q_i (mA h g^{-1})	Q_i 4 V (mA h g^{-1})	Q_i 5 V (mA h g^{-1})	Coulombic efficiency (%)
SG	90	70	20	75	69	6	83
Imp_1	79	54	25	70	58	12	89
Imp_2	72	48	24	69	57	12	95
TM	103	80	23	65	59	6	63
SS	65	50	15	55	49	6	85

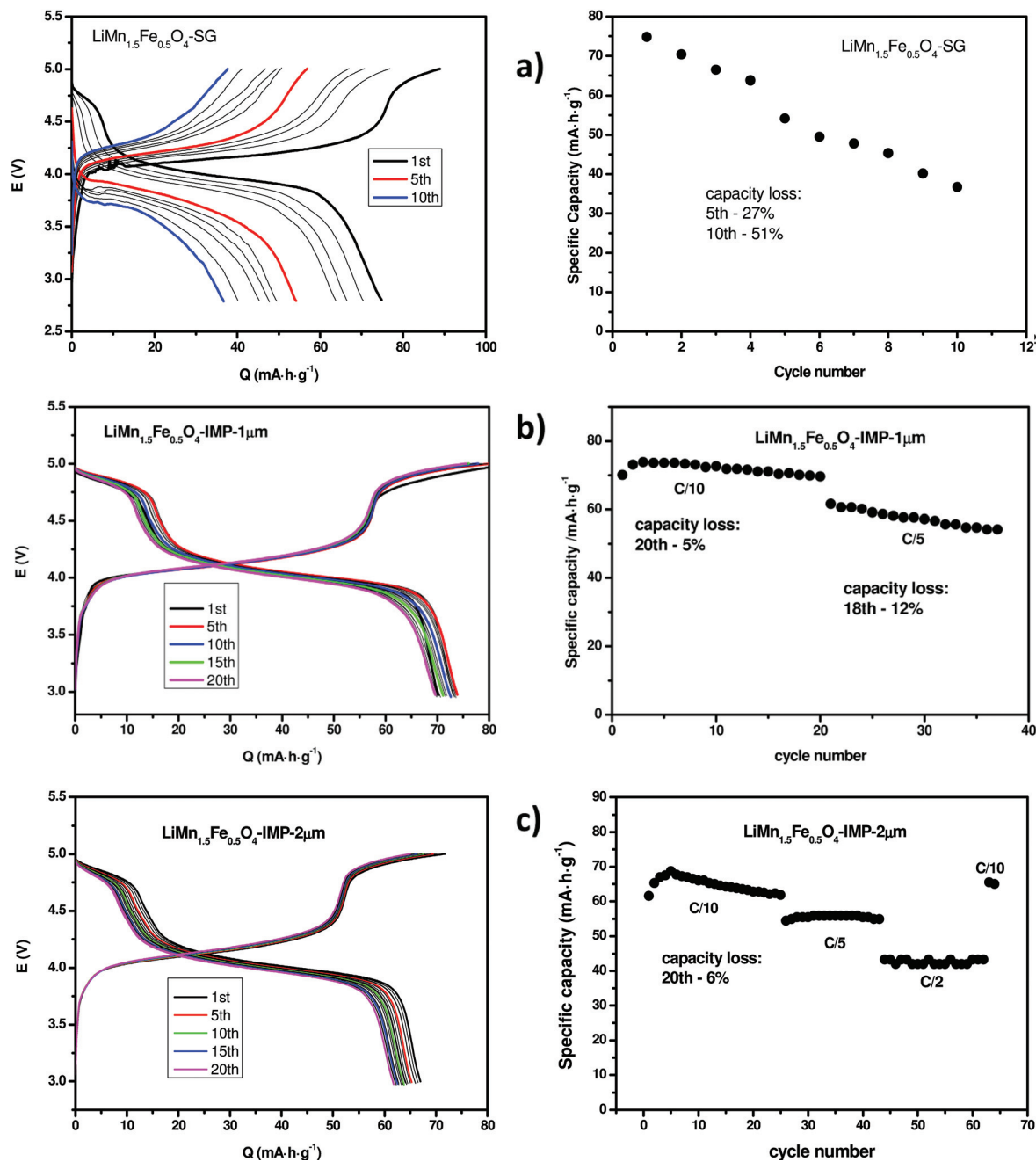


Fig. 6 Charge/ discharge curves at a rate C/10 for $\text{LiMn}_{1.5}\text{Fe}_{0.5}\text{O}_4$ prepared by different methods (left); and variations of the discharge capacity during various cycles when cycled between 5 and 3 V at different capacity rates (right). Capacity losses have been included in the graph. Charge/discharge curves at a rate C/10 for $\text{LiMn}_{1.5}\text{Fe}_{0.5}\text{O}_4$ prepared by different methods (left); and variations of the discharge capacity during various cycles when cycled between 5–3 V at different capacity rates (right). Capacity losses have been included in the graph.

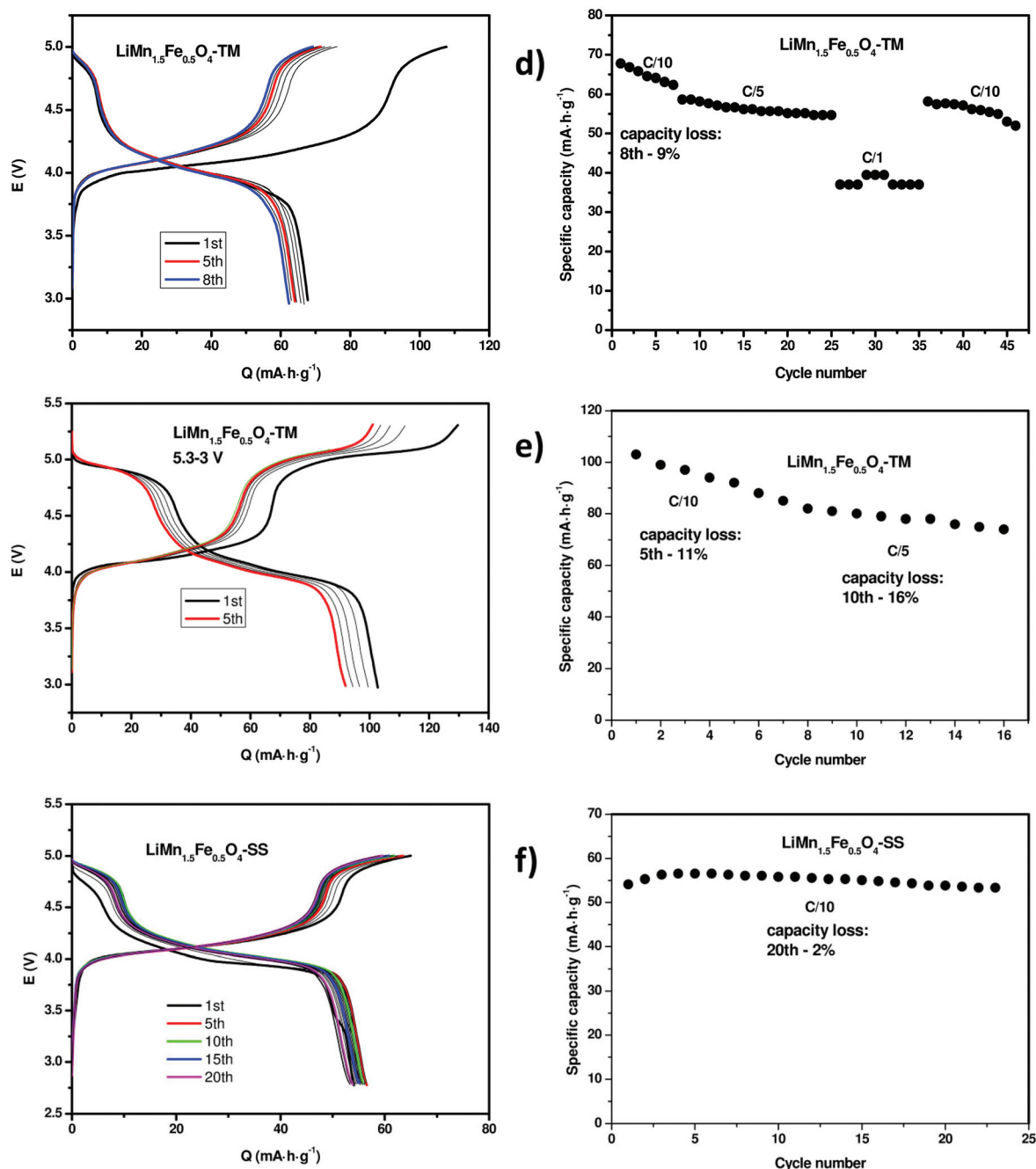


Fig. 6 (Contd.)

In order to evaluate the differences between electrochemical behaviours of spherical and rod morphologies, charge-discharge profiles for the $\text{LiFe}_{0.5}\text{Mn}_{1.5}\text{O}_4$ -TM sample have been obtained.

Fig. 6d (right) shows the discharge capacity *versus* the number of cycles for the electrodes with $\text{LiFe}_{0.5}\text{Mn}_{1.5}\text{O}_4$ cathode obtained by TM method (TM sample). It is interesting to observe that the discharge capacity only decreases slightly before 40 cycles at the lowest rates. If the cell is cycled at higher rates like C/1, the plateau of 5 V tends to disappear and the capacity decreases drastically. This fact suggests that the

insertion/deinsertion kinetic determines the extension of the plateau. It is worth mentioning that in this sample, the 5 V plateau at low rate is not affected, and it is even recovered at the end (see Fig. S10†). However, the extension of this plateau is very low and we have increased the highest limit of voltage up to 5.3 V for this sample. The results of these electrochemical tests are shown in Fig. 6e.

Although higher capacity values have been obtained when the voltage limit was 5 V, the capacity loss was also higher, even at low rates. Therefore, we can conclude that the electrolyte/electrode surface is modified by high-valent Fe. By com-

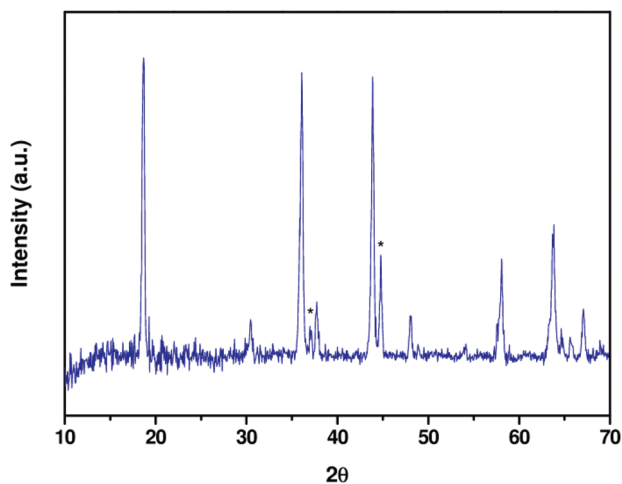


Fig. 7 X-Ray diffraction pattern of $\text{LiMn}_{1.5}\text{Fe}_{0.5}\text{O}_4/\text{Li}_2\text{MnO}_3$ composite. The maxima corresponding to Li_2MnO_3 are marked with asterisks.

paring the electrochemical profiles for Imp and TM samples, it is clear that the first sample shows a greater extension of the highest voltage plateau. Therefore, the spherical particles built by other nanometric units seem to help the insertion/deinsertion kinetics.

We would like to highlight the results obtained for the samples prepared by the SS method, in which after the 20th cycle the capacity loss is only of 2%. (Fig. 6f). Between the first and 5th cycles, the capacities increase and from here on losses are very small. This fact could be related to the possible existence of a small amount of Li_2MnO_3 , not observed in the X-ray diffraction pattern, but coherent with the low Mn:Fe ratio obtained for this sample (see Table 1). In this respect, it has been pointed out that in the $\text{LiMn}_{1.5}\text{Ni}_{0.5}\text{O}_4$ spinel and in Li_2MnO_4 layer composites cathodes, the capacity and energy density gradually increase during 50 cycles with a change in the shape of the charge–discharge profiles.³¹

In order to corroborate this hypothesis in our system, a cathode made of $\text{LiMn}_{1.5}\text{Fe}_{0.5}\text{O}_4/\text{Li}_2\text{MnO}_3$ composite was pre-

pared by the SS method (adding an adequate excess of lithium nitrate). The XRD pattern for this composite is given in Fig. 7, where the characteristic Li_2MnO_3 peaks are strongly defined (as shown with asterisks in Fig. 7).

Lee *et al.*,³¹ by means of *ex situ* XRD data analyses, stated that the entire Li_2MnO_3 layered phase transforms irreversibly into a cubic spinel phase in the composite cathode during extended electrochemical cycling. The new spinel phase consists of Mn and Ni in the 4+ oxidation state; therefore, such a spinel phase can only insert lithium (into the empty 16c octahedral sites) in the 3 V region without any plateau in the 4 or 4.7 V region. The electrochemical profile for the $\text{LiMn}_{1.5}\text{Fe}_{0.5}\text{O}_4/\text{Li}_2\text{MnO}_3$ composite cathode at C/10 is depicted in Fig. 8. The specific capacity increased slightly up to the 5th cycle and from there, a profile change is observed below 3.5 V; thus, the capacity continues to grow up to the 20th cycle. During extended electrochemical cycling at different current densities (Fig. S11[†]), the 4 and 5 V plateaus are smaller. This fact could be interpreted taking into account that the $(1-x)$ $\text{LiMn}_{1.5}\text{Fe}_{0.5}\text{O}_4/x\text{Li}_2\text{MnO}_3$ composite changes into the lithium-rich spinel phase $\text{Li}[\text{Li}_x\text{Fe}_{(1-x)/2}\text{Mn}_{(3-x)/2}]\text{O}_4$, in which a part of the 16d octahedral sites of the spinel phase are occupied by lithium ions.³² With the purpose to prove this idea in the future, complementary electrochemical experiments on this composite phase in the voltage window between 5 and 2 V should be of interest.

Finally, the coulombic efficiency is shown in Fig. 9 for all the samples. The difference between discharge and charge capacity is around 90%; therefore, the specific capacities reached are very similar in charge and discharge stages. As it can be observed, the coulombic efficiency remains constant along the tested cycles.

Regarding the single samples obtained, it is clear that microstructural morphology and electrochemical response are correlated. Through this study, the synthesis of these spinel cathodes by soft chemistry processes leading to different precursors is revealed as an effective route to modulate the final electrochemical behaviour. The responses of the nano and

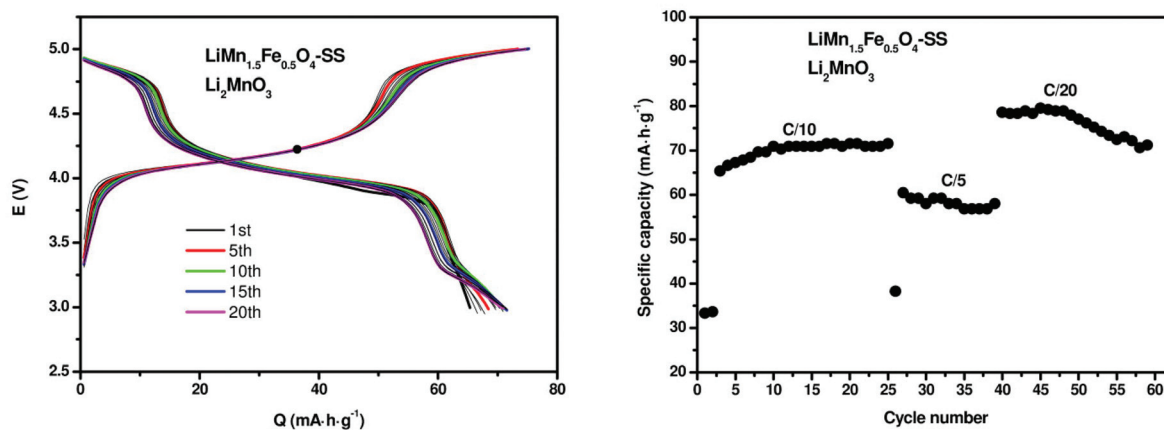


Fig. 8 Charge/discharge curves at a rate C/10 for $\text{LiMn}_{1.5}\text{Fe}_{0.5}\text{O}_4/\text{Li}_2\text{MnO}_3$ composite cathode (left); and variations of the discharge capacity during various cycles when cycled between 5.3–3 V at different capacity rate (right).

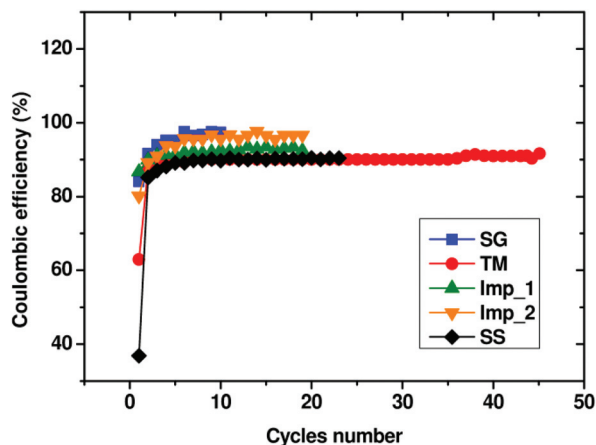


Fig. 9 Coulombic efficiency vs. cycles number at C/10.

microstructured samples synthesized in this work are improved compared to those of the SG phase, obtained by a more conventional sol-gel method. Though texture features as porosity seem not to affect appreciably the performance, other microstructural aspects do have a relevant role. Both hierarchical assembling and microstructure homogeneity influence the charge/discharge processes. In this sense, the samples composed of particles as nanostructured unities, with high uniformity in size and morphology (Imp_1, Imp_2), present an optimized response concerning cycling efficiency and capacity.

4. Conclusions

In this paper, a morphology-controlled synthesis of $\text{LiFe}_{0.5}\text{Mn}_{1.5}\text{O}_4$ spinels by different methods: sol-gel (SG), impregnation (Imp), template-hydrothermal (TM) and solvothermal (SS) is presented. The relationships among their textural, structural, morphological, and electrochemical properties are also reported. Although the textural characteristics are very similar for all the samples, different morphologies (microspheres, microrods and aggregates) and sizes were observed. Galvanostatic charge/discharge between 3 and 5 V at C/10 rate shows two plateaux at 4 and 5 V, related to the $\text{Mn}^{4+}/\text{Mn}^{3+}$ and $\text{Fe}^{4+}/\text{Fe}^{3+}$ couples. The highest specific capacity values were obtained at a voltage window up to 5.3 V, although the specific capacity loss became more important and the electrolyte/electrode surface was modified by high-valent Fe. Despite that, in all cases the coulombic efficiency is around 90% and remains constant along the tested cycles.

Stable specific capacities were achieved during various cycles in several samples, mainly in those obtained by impregnation, template and solvothermal synthesis. Thus, these samples show between 91% and 98% capacity retention after 20 cycles compared to 49% retention for the sample obtained by the more conventional sol-gel method. Moreover, the cells showed a good rate capability with average discharge capacity of 65, 55, and 44 mA h g^{-1} at current densities of C/10, C/5, and C/2, respectively. While altering the current density back

to C/10, a discharge capacity as high as 65 mA h g^{-1} could be recovered. Furthermore, a $\text{LiMn}_{1.5}\text{Fe}_{0.5}\text{O}_4/\text{Li}_2\text{MnO}_3$ composite was prepared by solvothermal process in order to increase the capacity and energy density to obtain satisfactory results. Again, when the current density returned to C/10 the discharge capacity was recovered by the cell.

Glossary

DEC	Diethyl carbonate
Dp	Pore diameter
EC	Ethylene carbonate
EDX	X-ray spectroscopy analysis
EG	Ethylene glycol
Imp	Impregnation
Q_D	Experimental specific capacities of deinsertion
Q_i	Experimental specific capacities of insertion
SEM	Scanning electron microscopy
SG	Sol-gel method
SS	Solvothermal synthesis
TG	Thermogravimetric
TM	Template-hydrothermal
Vp	Pore volume
XRD	X-Ray diffraction

Acknowledgements

Authors are grateful to the CAI centers of the UCM (XRD and electron microscopy) and financial support from Spanish Ministerio de Ciencia e Innovación, Grants MAT2010-20117.

References

- 1 S. S. Zhang, *J. Power Sources*, 2006, **161**, 1385.
- 2 S. S. Zhang, K. Xu and T. R. Jow, *J. Power Sources*, 2006, **160**, 1403.
- 3 M. Michalska, L. Lipińska, R. Diduszko, M. Mazurkiewicz, A. Małolepszy, L. Stobinski and K. J. Kurzydłowski, *Phys. Status Solidi C*, 2011, **8**, 2538.
- 4 A. Iturrondobeitia, A. Goñi, V. Palomares, I. Gil de Muro, L. Lezama and T. Rojo, *J. Power Sources*, 2012, **216**, 482.
- 5 J. M. Tarascon, *Philos. Trans. R. Soc. London, Ser. A*, 2010, **368**, 3227.
- 6 L. Xiong, Y. Xu, T. Tao and J. B. Goodenough, *J. Power Sources*, 2012, **199**, 214.
- 7 K. Ariyoshi, E. Iwata, M. Kuniyoshi, H. Wakabayashi and T. Ohzuku, *Electrochem. Solid State*, 2006, **9**, A557.
- 8 R. Thirunakaran, A. Sivashanmugam, S. Gopukumar and R. Rajalakshmi, *J. Power Sources*, 2009, **187**, 565.
- 9 J. Cho and B. Park, *Electrochem. Solid State*, 2000, **3**, 355.
- 10 M. M. Thackeray, *Prog. Solid State Chem.*, 1997, **25**, 1.
- 11 S. Dou, *J. Solid State Electrochem.*, 2013, **17**, 911.

- 12 S. Patoux, L. Sannier, H. Lignier, Y. Reynier, C. Bourbon, S. Jouanneau, F. Le Cras and S. Martinet, *Electrochim. Acta*, 2008, **53**, 4137.
- 13 J. E. Park, K. Kim, S. H. Park, E. S. Park, M. W. Pyeon and M. J. Lee, *Int. J. Electrochem. Sci.*, 2013, **8**, 6220.
- 14 A. Eftekhari, *J. Power Sources*, 2003, **124**, 182.
- 15 A. Eftekhari, *J. Power Sources*, 2004, **132**, 240.
- 16 A. Mas, M. L. López, I. Álvarez-Serrano, C. Pico and M. L. Veiga, *Dalton Trans.*, 2013, **42**, 9990.
- 17 L. Zhou, D. Zhao and X. W. Lou, *Angew. Chem., Int. Ed.*, 2012, **51**, 239.
- 18 J. Fei, Y. Cui, X. Yan, W. Qi, Y. Yang, K. Wang, Q. He and J. Li, *Adv. Mater.*, 2008, **20**, 452.
- 19 X. Wang and Y. Li, *J. Am. Chem. Soc.*, 2002, **124**, 2880.
- 20 L. Hu, H. Zhong, X. Zheng, Y. Huang, P. Zhang and Q. Chen, *Sci. Rep.*, 2012, **2**, 986.
- 21 D. Larcher, G. Sudant, R. Patrice and J. M. Tarascon, *Chem. Mater.*, 2003, **15**, 3543.
- 22 P. F. Fuls, L. Rodrigue and J. J. Fripiat, *Clays Clay Miner.*, 1970, **18**, 53.
- 23 J. Rodriguez-Carvajal, *Abstracts of the Satellite Meeting on Powder Diffraction of the XV Congress of the IUCr*, Toulouse, France, 1990, p. 127.
- 24 H. Tan, J. Verbeeck, A. Abakumov and G. Van Tendeloo, *Ultramicroscopy*, 2012, **116**, 24.
- 25 A. Laurence, J. Garvie, J. Thomas, J. Zega, P. Rez and P. R. Buseck, *Am. Mineral.*, 2004, **9**, 1610.
- 26 N. Kang, J. H. Park, J. Choi, J. Jin, J. Chun, I. G. Jung, J. Jeong, J. G. Park, S. M. Lee, H. J. Kim and S. U. Son, *Angew. Chem., Int. Ed.*, 2012, **51**, 6626.
- 27 J. B. Goodenough and Y. Kim, *Chem. Mater.*, 2010, **22**, 587.
- 28 T. Ohzuku, K. Ariyoshia, S. Takedaa and Y. Sakaib, *Electrochim. Acta*, 2001, **46**, 2327.
- 29 H. Bouayad, Z. Wang, N. Dupré, R. Dedryvère, D. Foix, S. Franger, J. F. Martin, L. Boutafa, S. Patoux, D. Gonbeau and D. Guyomard, *J. Phys. Chem. C*, 2014, **118**, 4634.
- 30 C. Marino, A. Darwiche, N. Dupre, H. Wilhelm, B. Lestriez, H. Martinez, R. Dedryvere, W. Zhang, F. Ghamouss, D. Lemordant and L. Monconduit, *J. Phys. Chem. C*, 2013, **117**, 19302.
- 31 E. S. Lee, A. Huq, H. Y. Chang and A. Manthiram, *Chem. Mater.*, 2012, **24**, 600.
- 32 B. Xu, C. R. Fell, M. Chi and Y. S. Meng, *Energy Environ. Sci.*, 2011, **4**, 2223.